On the Response of the Aleutian Low to Greenhouse Warming

BOLAN GAN,[a] LIXIN WU,[a] FAN JIA,[b] SHUJUN LI,[a] WENJU CAI,[a,c] HISASHI NAKAMURA,[d]
MICHAEL A. ALEXANDER,[e] AND ARTHUR J. MILLER[f]

[a] *Physical Oceanography Laboratory/CIMST, Ocean University of China and Qingdao
National Laboratory for Marine Science and Technology, Qingdao, China*
[b] *Key Laboratory of Ocean Circulation and Waves, Institute of Oceanology, Chinese
Academy of Sciences, Qingdao, China*
[c] *CSIRO Oceans and Atmosphere Flagship, Aspendale, Victoria, Australia*
[d] *Research Center for Advanced Science and Technology, University of Tokyo, Tokyo, Japan*
[e] *NOAA/Earth System Research Laboratory, Boulder, Colorado*
[f] *Scripps Institution of Oceanography, La Jolla, California*

ABSTRACT

Past and future changes in the Aleutian low are investigated by using observation-based sea level pressure (SLP) datasets and CMIP5 models. It is found that the Aleutian low intensity, measured by the North Pacific Index (NPI), has significantly strengthened during the twentieth century, with the observed centennial trend double the modeled counterpart for the multimodel average of historical simulations, suggesting compound signals of anthropogenic warming and natural variability. As climate warms under the strongest future warming scenario, the climatological-mean Aleutian low will continue to intensify and expand northward, as manifested in the significant decrease (-1.3 hPa) of the multimodel-averaged NPI, which is 1.6 times its unforced internal variability, and the increase in the central area of low pressure (SLP < 999.0 hPa), which expands about 7 times that in the twentieth century. A suite of idealized experiments further demonstrates that the deepening of the Aleutian low can be driven by an El Niño–like warming of the tropical Pacific sea surface temperature (SST), with a reduction in the climatological-mean zonal SST gradient, which overshadows the dampening effect of a weakened wintertime land–ocean thermal contrast on the Aleutian low change in a warmer climate. While the projected deepening of Aleutian low on multimodel average is robust, individual model portrayals vary primarily in magnitude. Intermodel difference in surface warming amplitude over the Asian continent, which is found to explain about 31% of the variance of the NPI changes across models, has a greater contribution than that in the spatial pattern of tropical Pacific SST warming (which explains about 23%) to model uncertainty in the projection of Aleutian low intensity.

1. Introduction

As one of the main centers of action in the atmospheric circulation over the Northern Hemisphere, the Aleutian low is a semipermanent low pressure system at the surface centered over the Aleutian Islands chain (Fig. 1a). The central pressure is lowest in boreal winter and nearly vanishing in summer. The Aleutian low is associated with powerful cyclones, which considerably affect local surface temperature and formation of pack ice in the Bering Sea (e.g., Overland and Pease 1982; Rodionov et al. 2005). It also closely links with upper-level teleconnections (Overland et al. 1999), such as the Pacific–North American teleconnection (PNA) and the

Arctic Oscillation, which are the dominant modes of atmospheric circulation. The Aleutian low thus plays a fundamental role in regulating winter climate of the North Pacific and the North American continent (e.g., Trenberth and Hurrell 1994; Deser et al. 2004). Furthermore, changes in the Aleutian low substantially affect the North Pacific oceanic gyres and upper-ocean temperature field, owing to the influence of wind stress curl and thermal forcing (e.g., Seager et al. 2001; Kwon and Deser 2007; Pickart et al. 2009), which can thereby alter fish stocks in the northeast Pacific (e.g., Hollowed et al. 2001; Chavez et al. 2003; Lehodey et al. 2006). Variations of the Aleutian low are related not only directly to decadal climate variability over the North Pacific (e.g., Latif and Barnett 1994; Schneider and Cornuelle 2005), but also remotely to the tropical

a)

Climatology of Aleutian Low

b)

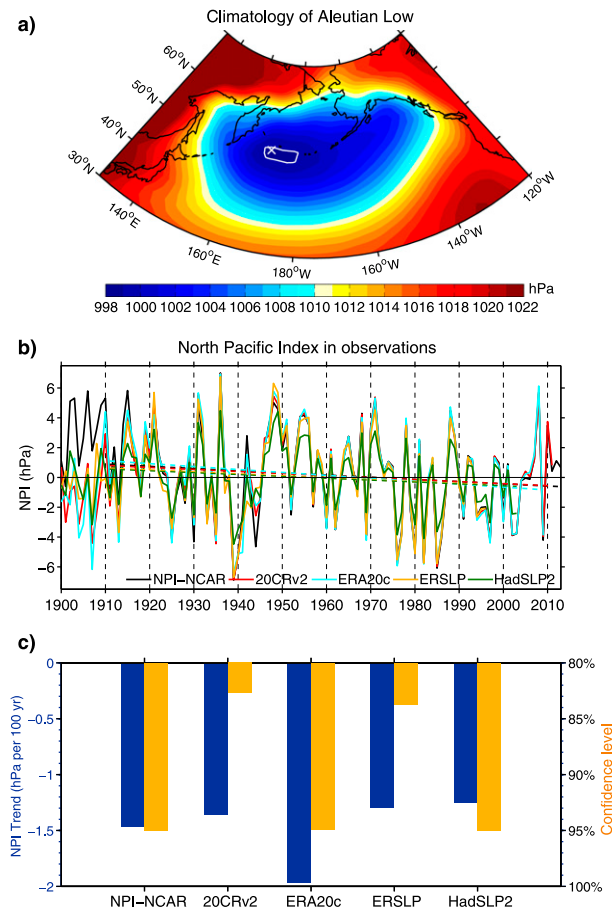North Pacific Index in observations

c)

FIG. 1. (a) The climatological-mean of winter SLP from 1950 to 1999 based on the 20CRv2 reanalysis data. A cross marks the minimum SLP of 998.8 hPa and solid contour denotes the isobar of 999.0 hPa. (b) The observed NPIs relative to the mean over the period of 1950–99 derived from five observation-based SLP datasets, except for 1950–1996 used for the ERSLP dataset. Dashed lines signify the long-term trend calculated from 1911 to the last year of the available SLP data for each dataset. (c) The centennial trends of the observed NPIs in five datasets and their confidence levels, estimated by the Sen median slope and the modified Mann–Kendall trend test, respectively. Note that the negative NPI indicates a relatively stronger Aleutian low.

interannual El Niño–Southern Oscillation (ENSO; Alexander et al. 2002).

Observational evidence indicates that the Aleutian low has strengthened since the late 1970s, based on the sea level pressure (SLP) reanalysis spanning the second half of the twentieth century (e.g., Gillett et al. 2003; Lu et al. 2004; Deser and Phillips 2009). The intensified basin-scale cyclonic flow associated with this stronger Aleutian low brings colder and drier air to the western North Pacific, and the reverse to the eastern North Pacific, resulting in decreased precipitation over coastal Asia and increased precipitation over southern Alaska as well as the southwestern United States (Deser et al. 2004; Honda et al. 2005).

Furthermore, the multidecadal shift of winter SLP over the Northern Hemisphere has been found to influence land surface warming during 1965–2000 (Wallace et al. 2012). However, there is no clear consensus on the relative importance of anthropogenic warming and natural variability in the dynamical contribution of the changing atmospheric circulation to land surface warming, since most climate models are deficient in reproducing the concurrent SLP variations (Gillett et al. 2005; Wallace et al. 2012). In other words, beyond the multidecadal enhancement of the Aleutian low, its long-term change over the twentieth century remains unknown.

Early modeling studies have mentioned an anomalously deepened Aleutian low pressure center under greenhouse gas forcing (e.g., Meehl and Washington 1996; Boer et al. 2000; Salathé 2006). However, detecting robust greenhouse warming signals in the changing Aleutian low is challenging since the relatively large internal variability of extratropical atmosphere introduces substantial uncertainty in the externally forced change (Xie et al. 2015). Deser et al. (2012) and Oshima et al. (2012) suggest that the internal climate variability primarily contributes to the total uncertainty in the projected change of SLP during the first half of the twenty-first century. In addition to the atmospheric internal variability, different responses of drivers of the Aleutian low variation to greenhouse forcing may lead to distinctions in the Aleutian low projection. One of the important drivers is the tropical Pacific sea surface temperature (SST), with El Niño–induced warm SST anomalies in the eastern tropical Pacific corresponding to a strengthened Aleutian low (Alexander et al. 2002). Climate models seem to suggest an enhanced SST warming in the eastern tropical Pacific under greenhouse warming (e.g., An et al. 2012; Yeh et al. 2012), but various reconstructed SST datasets spanning the twentieth century demonstrate diverse warming trends (Deser et al. 2010a). Besides, the winter land–ocean thermal contrast seems to be weakened in a warming climate, which may facilitate a weakened Aleutian low. Therefore, it remains uncertain how robustly the climatological-mean Aleutian low responds to greenhouse warming and what driving mechanisms are involved. Here, we investigate the twentieth-century long-term changes in the Aleutian low intensity based on five different observation-based SLP datasets and CMIP5 multimodel historical simulations, and its twenty-first-century projected response to greenhouse forcing under the RCP8.5 scenario. The possible driving mechanism is explored by a suite of idealized experiments with an intermediate climate model. We also investiage uncertainty in the winter SLP projection over the North Pacific among CMIP5 models and the influence of Arctic sea ice loss on the winter SLP projection.

TABLE 1. List of 22 CMIP5 models analyzed in this study. (Expansions of acronyms are available online at http://www.ametsoc.org/PubsAcronymList.)

Model name	Institute	Country
ACCESS1.0	Commonwealth Scientific and Industrial Research Organization/Bureau of Meteorology	Australia
BCC-CSM1.1	Beijing Climate Center, China Meteorological Administration	China
CanESM2	Canadian Centre for Climate Modeling and Analysis	Canada
CCSM4	National Center for Atmospheric Research	United States
CNRM-CM5	Météo-France/Centre National de Recherches Météorologiques	France
CSIRO-Mk3.6.0	Commonwealth Scientific and Industrial Research Organization/Queensland Climate Change Centre of Excellence	Australia
FGOALS-g2	Institute of Atmospheric Physics, Chinese Academy of Sciences	China
GFDL-CM3	National Oceanic and Atmospheric Administration/Geophysical Fluid Dynamics Laboratory	United States
GFDL-ESM2G		
GFDL-ESM2M		
GISS-E2-H	National Aeronautics and Space Administration/Goddard Institute for Space Studies	United States
GISS-E2-R		
HadGEM2-CC	Met Office Hadley Centre	United Kingdom
HadGEM2-ES		
INM-CM4	Institute for Numerical Mathematics	Russia
IPSL-CM5A-MR	Institute Pierre Simon Laplace	France
IPSL-CM5B-LR		
MIROC-ESM	University of Tokyo, Atmosphere and Ocean Research Institute; National Institute for Environmental Studies; Japan Agency for Marine Earth Science and Technology	Japan
MPI-ESM-LR	Max Planck Institute for Meteorology	Germany
MPI-ESM-MR		
MRI-CGCM3	Meteorological Research Institute	Japan
NorESM1-M	Norwegian Climate Centre	Norway

The rest of the paper is organized as follows. Section 2 briefly describes the datasets, methods, and an intermediate climate model (CAM3.1-RGO). Section 3 characterizes the long-term change in Aleutian low intensity during the past century and its projected change in future. Section 4 presents the driving mechanism for the Aleutian low response, which is demonstrated by the idealized experiments. Section 5 analyzes model uncertainty in the winter SLP projection over the North Pacific. Discussion and a summary are given in sections 6 and 7, respectively.

2. Datasets and methods

a. Observation-based NPI in the twentieth century

In this study, the Aleutian low intensity is represented by the North Pacific Index (NPI), which is defined as the area-weighted average of winter [December–February (DJF)] SLP over the region bounded by 30°–65°N and 160°E–140°W (Trenberth and Hurrell 1994). Centennial-long NPIs are constructed from five historical observation-based SLP datasets. The monthly NPI data are available online at https://climatedataguide.ucar.edu/climate-data/north-pacific-np-index-trenberth-and-hurrell-monthly-and-winter, which is derived from the National Center for Atmospheric Research's SLP dataset (NPI-NCAR;

Trenberth and Paolino 1980). The other four monthly SLP datasets include two reanalysis datasets [i.e., the National Oceanic and Atmospheric Administration (NOAA)/Cooperative Institute for Research in Environmental Sciences Twentieth Century Reanalysis version 2 (20CRv2; $2° \times 2°$ resolution; Compo et al. 2011) and the newly developed European Centre for Medium-Range Weather Forecasts (ECMWF) Twentieth Century Reanalysis (ERA20c; $1° \times 1°$ resolution; Poli et al. 2016)] and two reconstruction datasets [i.e., the NOAA Extended Reconstructed SLP (ERSLP; $2° \times 2°$ resolution; Smith and Reynolds 2004) and the Met Office Hadley Centre's SLP dataset version 2 (HadSLP2; $5° \times 5°$ resolution; Allan and Ansell 2006)].

b. CMIP5 multimodel outputs

The simulated SLP, SST, surface air temperature (SAT), and sea ice concentration (SIC) field are taken from 22 climate models participating in CMIP5 (Table 1; Taylor et al. 2012), organized by the Program for Climate Model Diagnosis and Intercomparison for the Intergovernmental Panel on Climate Change Fifth Assessment Report. We analyzed three sets of simulations: the preindustrial control simulations that represent the natural variability of climate system with atmospheric CO_2 concentration fixed at 280–290 ppm, the historical

simulations that incorporate the anthropogenic and natural forcings from the observed atmospheric composition changes in the twentieth century, and the future projections under the RCP8.5 scenario that are characterized by an escalating radiative forcing throughout the twenty-first century (reaching approximately 8.5 Wm^{-2} in 2100; equivalent to atmospheric CO_2 concentration exceeding 1370 ppm). Only one member (r1i1p1) run for each model is used in this study. We interpolated model outputs to a common 1° × 1° grid for SST and SIC, and 2° × 2° grid for SLP and SAT. Note that, in each model, the 50-yr-interval difference of all variables in winter (DJF) between the RCP8.5 run (2050–99) and the historical run (1950–99) is considered as the projected response to greenhouse warming.

c. CAM3.1-RGO model

We performed a suite of idealized experiments with an intermediate climate model (CAM3.1-RGO) that is a fully coupled system consisting of the Community Atmosphere Model version 3 (CAM3.1; Collins et al. 2006) and a 1.5-layer reduced-gravity ocean (RGO) model with flux corrections (Fang 2005). As part of the Community Climate System Model version 3 (CCSM3) developed at NCAR, CAM3.1 is based on an Eulerian spectral dynamical core, with a T42 horizontal resolution and 26 vertical levels. The 1.5-layer RGO model is an extended Zebiak–Cane type (Zebiak and Cane 1987; Clement et al. 1996), in which the active upper layer is divided into a fixed depth of mixed layer to simulate SST variation and a subsurface layer to parameterize the entrained subsurface temperature through the multivariate linear relationship with thermocline depth. This ocean model, containing variability off the equatorial band, covers a global domain (80°S–80°N, 0°–360°) with 1° latitude by 2° longitude resolution, which has been successfully used to study tropical oceanic processes and ENSO (e.g., Chiang et al. 2008; Jia and Wu 2013).

d. Trend estimation and correlation significance test

Long-term trend is estimated with the Sen median slope (Sen 1968), which is much less sensitive to outliers and skewed distributions than the conventional least squares fit. The corresponding statistical significance is assessed by the modified Mann–Kendall trend test, a nonparametric method with accounting for the autocorrelation of time series (Hamed and Rao 1998). All trends are scaled to the 100-yr change. Because the five observation-based NPIs pre-1910 are not consistent with each other (see Fig. 1b), we evaluated the centennial-trends of NPIs from 1911 to the last year of the available SLP data (i.e., 1911–2013 for NPI-NCAR, 1911–2011 for

20CRv2, 1911–2009 for ERA20c, 1911–96 for ERSLP, and 1911–2003 for HadSLP2).

Considering the small sample size, we examined the statistical significance of correlation coefficient with a nonparametric Monte Carlo test (Livezey and Chen 1983). Specifically, the correlation coefficient is calculated 1000 times with the time series of projected NPI change randomly scrambled. Then the probability distribution function of these 1000 correlation coefficients is constructed to rank the significance of the actual correlation. In fact, we also checked the Student's t test and found that the difference of significance P value between them is on the order of 10^{-3}.

e. Estimation of internal variability in CMIP5 models

Following Collins et al. (2013), unforced internal variability of climate system in CMIP5 models is estimated using at least 500-yr-long (after spinup period) outputs of preindustrial control simulations. We calculated nonoverlapping 20-yr means for each grid point, from which a quadratic fit as a function of time is subtracted to eliminate model drift. Variability for each grid point is then estimated as the standard deviation of that 20-yr means, which is further multiplied by the square root of 2 to account for the fact that the variability of a difference in means is expected due to unforced internal variability. The median of those quantities across models is used as the estimated internal variability.

3. Past and future changes in the Aleutian low

a. Long-term change in the twentieth century

First, we examined the long-term change in Aleutian low intensity during the twentieth century, based on NPIs constructed from five different observation-based SLP datasets drawn from reconstructions and reanalysis. As shown in Fig. 1b, all NPIs display coherent and significant interannual-to-multidecadal fluctuations (e.g., decadal transitions in the 1940s and 1970s), except for the period of 1900–10 in which NPIs are diverse from each other. Despite this short-term variability, a long-term downward trend can be perceived over the twentieth century, indicating an intensification of the Aleutian low. Figure 1c shows that the centennial-trend estimations of NPIs scaled to the 100-yr change are −1.5 hPa for NCAR-NPI, −1.9 hPa for ERA20c, −1.2 hPa for HadSLP2 (all significant at the 95% confidence level), and −1.4 hPa for 20CRv2 and −1.3 hPa for ERSLP (both significant at the 83% confidence level). Therefore, the NPI trend averaged over such five estimations is approximately −1.5 hPa throughout the twentieth century, with a 95% confidence interval of −1.1 to −1.9 hPa based on a two-tailed Student's t test. This NPI trend is approximately 16% of

TABLE 2. Centennial trends of NPIs in the twentieth century, derived from five observation-based SLP datasets and historical simulations of 22 CMIP5 models. Trend ($\pm$ significant interval of $P = 0.1$ based on a two-tailed Student's t test) is estimated by the least squares fit.

Observation-based datasets	Trend [hPa $(100 \, \mathrm{yr})^{-1}$]
NPI-NCAR	-1.79 ± 1.65
20CRv2	-1.33 ± 1.73
ERA20c	-1.89 ± 1.84
ERSLP	-1.63 ± 2.28
HadSLP2	-1.49 ± 1.38
Model name	Trend [hPa $(100 \, \mathrm{yr})^{-1}$]
ACCESS1.0	0.45 ± 1.40
BCC-CSM1.1	-0.88 ± 1.71
CanESM2	-2.99 ± 1.84
CCSM4	-1.64 ± 2.19
CNRM-CM5	0.43 ± 1.50
CSIRO-Mk3.6.0	-1.08 ± 1.65
FGOALS-g2	-0.61 ± 1.71
GFDL-CM3	-0.60 ± 1.68
GFDL-ESM2G	0.55 ± 1.91
GFDL-ESM2M	-0.70 ± 1.94
GISS-E2-H	-0.77 ± 1.29
GISS-E2-R	0.35 ± 1.37
HadGEM2-CC	-1.37 ± 1.39
HadGEM2-ES	-0.38 ± 1.37
INM-CM4	-2.11 ± 1.28
IPSL-CM5A-MR	-2.13 ± 2.10
IPSL-CM5B-LR	-0.95 ± 1.30
MIROC-ESM	0.17 ± 1.27
MPI-ESM-LR	-0.52 ± 1.42
MPI-ESM-MR	-0.97 ± 1.32
MRI-CGCM3	0.56 ± 1.39
NorESM1-M	0.66 ± 2.14

the climatological-mean zonal deviation of SLP over the North Pacific, defined as the deviation from the zonal mean pressure averaged between 30° and 65°N (i.e., $-9.2 \, \mathrm{hPa}$ for the reference period 1950–99). Note that we also checked the centennial trend of NPI estimated by the least squares fit. Table 2 shows that trend estimations are generally similar to that based on the Sen median slope, but the error intervals are comparable to trend magnitudes, which reflects the large winter-to-winter variation of NPI.

A natural question arises as to how well CMIP5 climate models simulate the variability and long-term trend of NPI in the twentieth century. Here we examined the simulated NPIs constructed from 22 multimodel SLP outputs of the historical simulations. Comparing Figs. 2a and 1a, the models can simulate the climatological-mean Aleutian low well, although the modeled minimum SLP is slightly lower by 0.1 hPa and displaced southeastward by 2° latitude and 10° longitude relative to that observed. However, the models generally lack the capability to capture the phase variation of

NPI in observation and most models underestimate its winter-to-winter standard deviation. As shown in Fig. 2b, the simulated NPIs in 22 models are largely diverse from each other, but still cover the observed NPI variation. Table 3 further suggests that 14 (7) out of 22 models underestimate (overestimate) the winter-to-winter standard deviation of NPI by ranging from 4% (5%) to 27% (50%) of the observed counterpart. Owing to the large intermodel spread, the multimodel ensemble mean (MMEM) time series of simulated NPIs (Fig. 2c) is substantially smoother than the observed NPI, with much lower standard deviation than that of NCAR-NPI (0.7 vs 3.1 hPa). Based on this MMEM time series of NPI, we detected a statistically significant downward trend, with the magnitude of $0.7 \, \mathrm{hPa} \, (100 \, \mathrm{yr})^{-1}$, which is about half of the aforementioned one in observation. However, it is noteworthy that when looking into the performance of each model (Fig. 2d), 16 out of 22 models are in agreement on the sign of downward centennial trend, but they vary with regard to the magnitude [a range of 0.1–$3.3 \, \mathrm{hPa} \, (100 \, \mathrm{yr})^{-1}$], such that only five models produce significant trends larger than or comparable to the observation.

The long-term change of NPI in the twentieth century involves the anthropogenically induced signal and the natural atmospheric variability, which is large in the wintertime (as reflected in the large error interval of trend in Table 2). Given that, the MMEM time series of NPI likely suppress the internal atmospheric variability under the assumption that each model represents a different realization of atmospheric variability. Therefore, such downward trend detected in the MMEM time series of NPI, as well as in observations, may reflect a deepening tendency of the climatological-mean Aleutian low in response to anthropogenic warming over the past century. But there is a large difference in the centennial-trend magnitude of NPI between historical simulations and observations, which is further discussed in section 6b.

b. Projected response to greenhouse warming in the twenty-first century

To better understand how the Aleutian low changes under external greenhouse forcing, we examined the 50-yr-interval NPI/SLP difference between the future projection under the RCP8.5 scenario and the historical simulation in each model. As shown in Fig. 3a, more than half the models exhibit significant changes of NPI, among which all except one agree on the sign of decreased NPI, indicating a deeper-than-normal Aleutian low. The MMEM of NPI changes shows a decrease of approximately $-1.3 \, \mathrm{hPa}$ (a 95% confidence interval of -0.7 to $-1.9 \, \mathrm{hPa}$), which is 62% larger than the unforced internal variability of NPI evaluated based on the
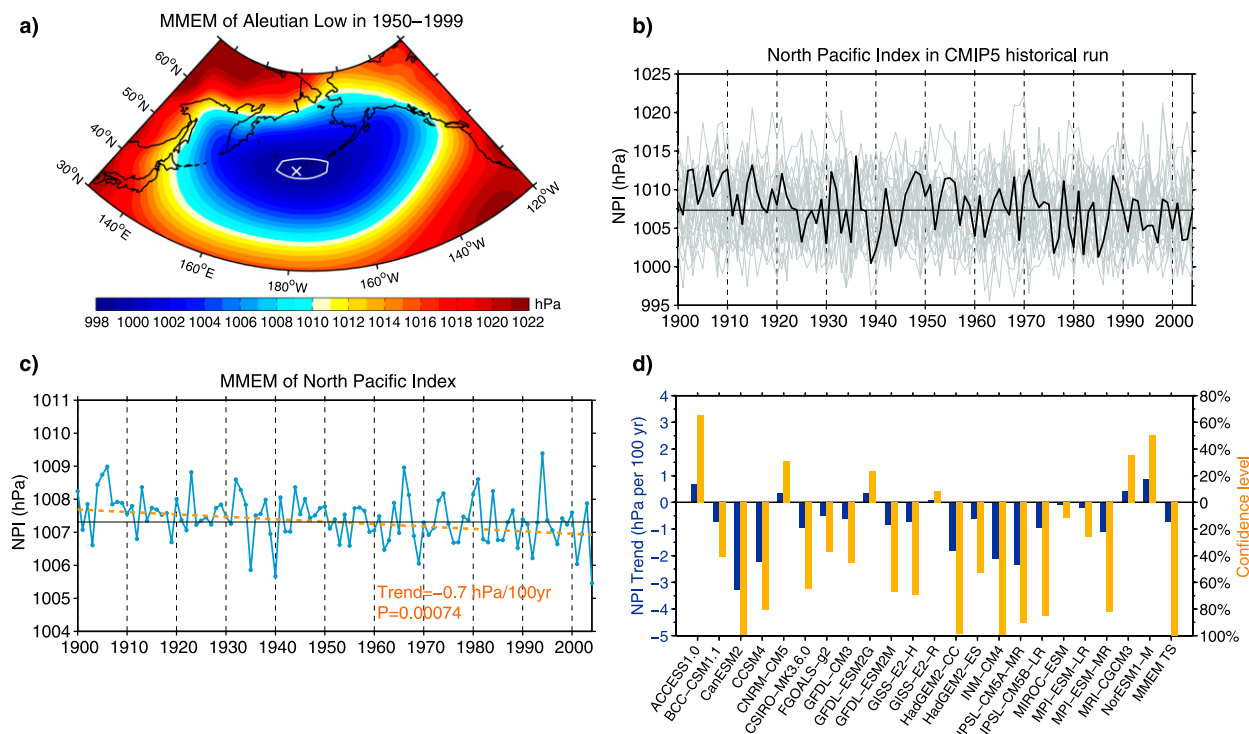
FIG. 2. (a) As in Fig. 1a, but for the CMIP5 MMEM of winter SLP in the historical run. A cross marks the minimum SLP of 998.7 hPa and solid contour denotes the isobar of 999.0 hPa. (b) The simulated NPIs in 22 models (gray curves) and NCAR-NPI (black curve). Black line denotes the NPI mean in 1950–99 (i.e., 1007.3hP), which is identical for NCAR-NPI and the multimodel average. (c) The MMEM time series of NPI in the historical run, superimposed on the long-term trend (dashed line), with respect to the 1950–99 reference period (black line). Note the different y axis between (b) and (c). (d) As in Fig. 1c, but for the simulated NPIs in 22 models as well as the MMEM time series of NPI. Trend is estimated from 1900 to 2004.

preindustrial control simulations (i.e., approximately 0.8 hPa; Table 3). This 50-yr-interval change of NPI is indeed almost identical to its long-term trend scaled to the 100-yr change during the twenty-first century (2006–99), which is higher than the corresponding winter-to-winter variability (i.e., the interannual standard deviation of the MMEM time series of the twenty-first-century NPI is 0.8 hPa). Further normalizing the NPI change by the global-mean surface temperature warming in each model and then taking MMEM, it shows that the scaled NPI change is approximately $-0.4 \, hPa \, {}^{\circ}C^{-1}$ (a 95% confidence interval of $-0.2 \, hPa \, {}^{\circ}C^{-1}$ to $-0.6 \, hPa \, {}^{\circ}C^{-1}$). More specifically, comparison of Figs. 3b and 2a shows that the central area of the Aleutian low in the twenty-first century, outlined by the isobar of 999.0 hPa, expands about 7 times that in the twentieth century, and the minimum SLP is decreased by 3.1 hPa. Here the isobar of 999.0 hPa is chosen as the threshold because it is the minimum isobar that can be profiled by all models. Overall, results suggest that the climatological-mean Aleutian low is significantly intensified as a consequence of greenhouse warming in the twenty-first century.

In regard to the projected response in space, the low pressure system is found to intensify and expand northward, as inferred from the spatial pattern of winter SLP change over the North Pacific. Figure 3c shows a southeastward-tilted pattern of the estimated internal variability of winter SLP, with one center of action of 1.6 hPa located over the Bering Sea and the other one of 1.5 hPa located over the eastern North Pacific. Under the greenhouse forcing, the low pressure system to north of 45°N except over the western coast of North American displays a highly robust intensification (stippling region in Fig. 3d), with the maximum decrease of SLP reaching -5.5 hPa over the northern Bering Sea, which is about 3.5 times the internal variability. This is accompanied with a slight increase of SLP along a zonal band extending from Japan to the central North Pacific, implying a northward shift of the Aleutian low, which has also been indicated in earlier studies with CMIP3 models (e.g., Hori and Ueda 2006; Salathé 2006). To be clear, we further analyzed change in the latitudinal position of the Aleutian low center in each model, which is defined as the location where SLP has a minimum within the region of 30°–65°N, 160°E–140°W. Table 4 shows

TABLE 3. Normalized standard deviation (dimensionless) and the estimated internal variability of NPI in CMIP5 model. Here the winter-to-winter standard deviation of NPI in each model is normalized by the observed counterpart averaged over five NPIs in Fig. 1 (i.e., 3.04 hPa).

Model name	Normalized STD	Internal variability (hPa)
ACCESS1.0	0.96	0.82
BCC-CSM1.1	1.00	0.76
CanESM2	1.12	0.81
CCSM4	1.50	0.68
CNRM-CM5	0.83	0.67
CSIRO-Mk3.6.0	1.05	0.87
FGOALS-g2	0.89	0.93
GFDL-CM3	0.93	1.11
GFDL-ESM2G	1.19	0.91
GFDL-ESM2M	1.28	1.11
GISS-E2-H	0.82	0.72
GISS-E2-R	0.83	0.76
HadGEM2-CC	0.86	0.68
HadGEM2-ES	0.78	1.18
INM-CM4	0.73	0.73
IPSL-CM5A-MR	1.24	1.08
IPSL-CM5B-LR	0.81	0.70
MIROC-ESM	0.82	0.67
MPI-ESM-LR	0.90	0.75
MPI-ESM-MR	0.87	0.72
MRI-CGCM3	0.80	0.89
NorESM1-M	1.37	0.80

that 12 out of 22 models display a northward movement, whereas 2 (8) of the rest display a southward movement (stationary behavior). Comparison of Figs. 3b and 2a also shows a northeastward displacement of the minimum SLP by 2° latitude and 2° longitude in response to greenhouse warming. It should be noted that the weak robustness of the MMEM SLP change over the band of 30°–45°N and the southeastern part of the North Pacific (see Fig. 3d) could result from smaller changes in individual models than the internal variability and/or high-level disagreement on the sign of change across models. Further inspection indicates, on average, a greater contribution from small changes for regions to east of 160°W, with 47% of models exhibiting small changes versus 35% of models disagreeing on the sign of MMEM change. However, for the rest (i.e., the region of 30°–45°N, 130°E–160°W), contributions from both of them are identical, with 16% of models displaying both aspects and an additional 23% of models displaying either aspect.

4. Possible driving mechanism for the intensified Aleutian low in a warmer climate

a. Land–ocean thermal contrast change

The Aleutian low is a surface manifestation of the atmospheric planetary-scale waves (Terada and Hanzawa 1984).

As can be seen from Fig. 4a, the zonal deviation of SLP, which depicts the stationary planetary waves, aligns well with the geographic distribution of climatological-mean SLP in winter. It has been demonstrated that large-scale topography and land–ocean heating contrast provide primary forcing for stationary waves in the troposphere, which is especially strong during the Northern Hemisphere cold season (Andrews et al. 1987). Specifically, air over the North Pacific Ocean is much warmer than over the Eurasian and North American continents in winter, which leads to a relatively large land–ocean thermal contrast (LOTC) and in turn partly forces the low pressure over the ocean. Given that, we investigated the relationship between responses of the Aleutian low and the winter LOTC to greenhouse warming by comparing changes in the NPI and the LOTC among models. Here the LOTC is estimated as the difference between SAT averaged over the North Pacific Ocean and the Asian continent, i.e., LOTC = SAT_{Ocean}(40°–60°N, 170°E–150°W) − SAT_{Land}(40°–60°N, 80°–120°E), which is positive for climatological mean. Such two select regions cover the centers of the zonal-deviation pattern of SLP (Fig. 4a) and the ''cold ocean–warm land'' pattern induced by the land–ocean distribution (Wallace et al. 1996).

As shown in Fig. 4b, all but one of the models project a weakening of the LOTC, with an MMEM decrease of −1.6°C (a 95% confidence interval of −1.1° to −2.1°C), suggesting a larger warming over the Asian continent compared to the North Pacific Ocean. Indeed, the MMEM ratio of SAT_{Land} warming to SAT_{Ocean} warming is 1.4. However, the majority of models (15/22) project the intensification of the Aleutian low coherently with the weakening of the thermal contrast, represented by decreases of the NPI and the LOTC, respectively. Changes in the NPI and the LOTC are significantly correlated among models, with correlation coefficient of −0.47 (P = 0.02). In particular, if two outliers with LOTC changes larger than −0.5 (i.e., FGOALS-g2 and GFDL-ESM2G) are excluded, the correlation coefficient reaches −0.74. It is suggested that models with a larger decrease in the LOTC tend to have a smaller decrease or even increase in the NPI. In other words, the weaker LOTC that arises in a warmer climate dampens the Aleutian low response to greenhouse warming. Therefore, the intensification of the Aleutian low must involve other processes that overwhelm such a negative effect of the weakened LOTC.

b. Tropical Pacific SST warming

As mentioned, variation of the tropical Pacific SST plays an important role in altering the Aleutian low, since El Niño events act to deepen the Aleutian low through the PNA teleconnection. A linkage between
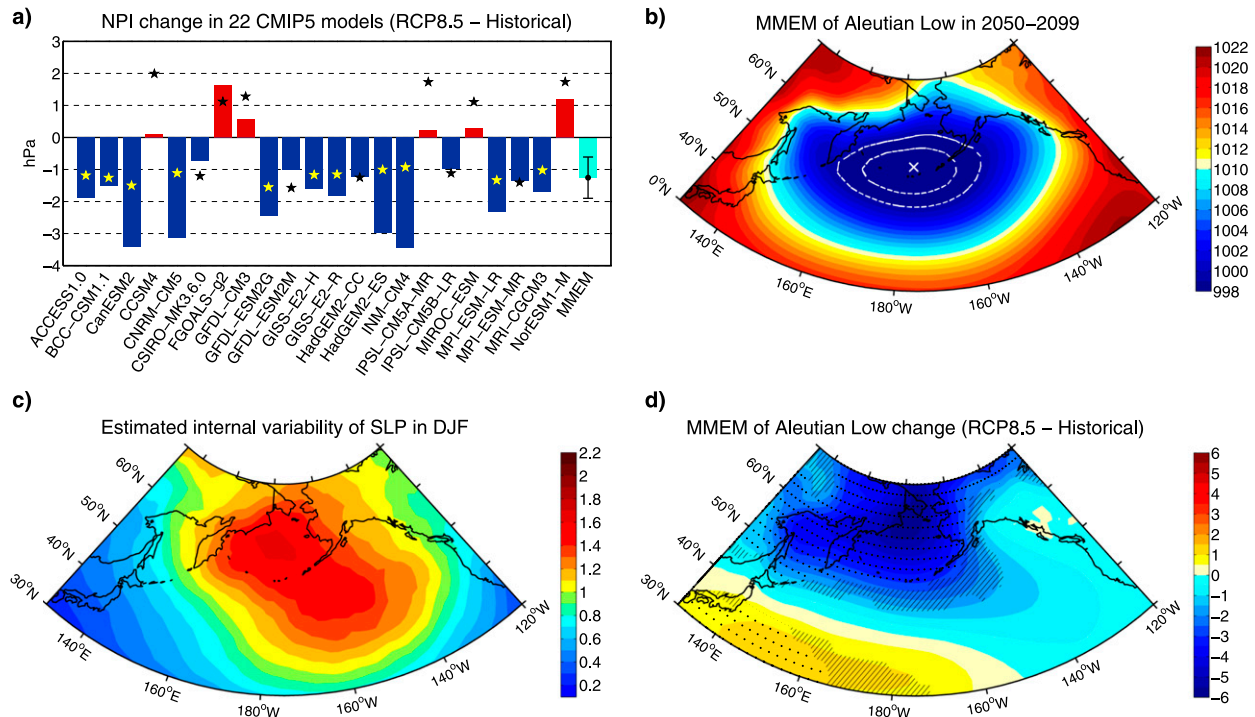
FIG. 3. (a) NPI changes in 22 CMIP5 models between the 50-yr RCP8.5 run and historical run. Asterisks (error bar) denote the 95% confidence level (interval) based on a two-tailed Student's *t* test. (b) The MMEM of winter SLP in the RCP8.5 run. A cross marks the minimum SLP of 995.5 hPa and dashed contours denote the isobars of 997.0 and 999.0 hPa. (c) The estimated internal variability of winter SLP based on the CMIP5 preindustrial control experiments. (d) The MMEM of winter SLP changes between the 50-yr RCP8.5 run and historical run. Stippling indicates regions where the MMEM change is greater than two standard deviations of internal variability and where at least 85% (19/22) of the models agree on the sign of change. Hatching indicates regions where the MMEM change is in the range of one to two standard deviations of internal variability. The rest are regions where the MMEM change is less than one standard deviation of internal variability.

changes in the extratropical SLP and the tropical Pacific Ocean under greenhouse forcing has also been implied (Meehl and Washington 1996; Boer et al. 2000; Yamaguchi and Noda 2006; Sueyoshi and Yasuda 2012). Given that, we turn to inspect the projected change in the tropical Pacific SST and its relationship with the intensification of the Aleutian low.

From Fig. 5a, it can clearly be seen that the CMIP5 projections exhibit large SST warming over the eastern equatorial Pacific (EEP; 5°S–5°N, 90°–150°W) in winter, with a maximum warming of 3.1°C predicted near the Galápagos Islands, which is higher than that over the western equatorial Pacific (WEP; 5°S–5°N, 120°–170°E). This indicates a reduction in the time-mean zonal SST gradient across the equatorial Pacific, which is referred as an El Niño–like warming (without implying a change in the El Niño variability). Notably, more than two-thirds (17/22) of the models produce an El Niño–like warming pattern of the tropical Pacific SST, as seen by the positive east–west warming differences across the equatorial Pacific [i.e., SST warming area-averaged in the EEP minus that in the WEP, denoted as

Δ(EEP SST) − Δ(WEP SST)] in the individual models (Fig. 5b). The MMEM for this difference is 0.3°C, with a 95% confidence interval of 0.1°C to 0.5°C. We further compared the NPI changes with Δ(EEP SST) − Δ(WEP SST) among models (Fig. 5b) and found that they are significantly correlated at −0.45 ($P = 0.04$). It is suggested that, on average, the larger the east–west SST warming differences across the equatorial Pacific, the stronger the Aleutian low intensity. Therefore, an El Niño–like SST warming pattern in the tropical Pacific is likely to be an important driver in the intensification of the Aleutian low and will continue to do so as the climate warms further. Next, we attempt to verify this conjecture by conducting a suite of idealized experiments with the CAM3.1-RGO model, considering that this model simulates a robust El Niño–like warming pattern of the tropical Pacific SST in response to the doubled CO_2 concentration ($2CO_2$) forcing (Jia and Wu 2013).

We first conducted a pair of multicentury integrations of CAM3.1-RGO fully coupled model: a 400-yr control run with the CO_2 concentration fixed at 360 ppm

TABLE 4. Latitudinal position of the Aleutian low center (i.e., minimum SLP over the North Pacific) in the historical and RCP8.5 runs as well as their difference.

Model name	Historical (°N)	RCP8.5 (°N)	Difference (°)
ACCESS1.0	56	54	−2
BCC-CSM1.1	52	54	2
CanESM2	54	54	0
CCSM4	54	54	0
CNRM-CM5	54	54	0
CSIRO-Mk3.6.0	48	50	2
FGOALS-g2	50	56	6
GFDL-CM3	50	52	2
GFDL-ESM2G	50	54	4
GFDL-ESM2M	54	54	0
GISS-E2-H	50	52	2
GISS-E2-R	50	52	2
HadGEM2-CC	50	52	2
HadGEM2-ES	56	52	−4
INM-CM4	54	54	0
IPSL-CM5A-MR	50	54	4
IPSL-CM5B-LR	48	48	0
MIROC-ESM	58	58	0
MPI-ESM-LR	50	52	2
MPI-ESM-MR	48	52	4
MRI-CGCM3	50	52	2
NorESM1-M	52	52	0

(CAM3.1-RGO-CTRL) and a 300-yr run under the quadrupled CO_2 concentration ($4CO_2$) forcing (CAM3.1-RGO-$4CO_2$) that integrates starting at the 100th year of CAM3.1-RGO-CTRL. Then we performed a suite of sensitivity experiments with the CAM3.1 stand-alone atmospheric model. CAM3.1 reasonably simulates the Aleutian low, although the modeled NPI is weaker than the observation by approximately 3 hPa (not shown). The sensitivity experiments consist of three runs: 1) a 100-yr control run with the CO_2 concentration fixed at 360 ppm (CAM3.1-CTRL), in which CAM3.1 is forced by the monthly SST fields derived from the last 200 years of CAM3.1-RGO-CTRL; 2) a 100-yr $4CO_2$ run with the CO_2 concentration fixed at 1460 ppm (CAM3.1–$4CO_2$), in which CAM3.1 is forced by the monthly SST fields derived from the last 200 years of CAM3.1-RGO-$4CO_2$; and 3) a 100-yr global uniform warming run with the CO_2 concentration fixed at 1460 ppm (CAM3.1–$4CO_2$-GUW), in which CAM3.1 is forced by the monthly and spatially uniform SST increase derived by adding the globally averaged SST warming difference between CAM3.1-RGO-$4CO_2$ and CAM3.1-RGO-CTRL (over the last 200 years) to the monthly SST field of CAM3.1-RGO-CTRL. In the CAM3.1–$4CO_2$-GUW run, the El Niño–like warming pattern is removed.

As for the response to quadrupled CO_2 concentration forcing, the CAM3.1-RGO coupled model produces a well-defined El Niño–like SST warming in the tropical Pacific, with an east–west warming difference of 1.5°C (Fig. 6a) and a strengthening of the Aleutian low as well as a weakening of the LOTC (similar to the result of CAM3.1–$4CO_2$ run), as in the majority of CMIP5 models. In the CAM3.1–$4CO_2$ run, the Aleutian low is intensified and expanded northward, which can be clearly seen from large decreases of SLP extending from the Bering Sea to the eastern North Pacific (Fig. 6b) and a significant reduction (−1.4 hPa) of NPI (Fig. 6d). However, when the El Niño–like warming pattern is removed, the Aleutian low is considerably weakened, manifested as a substantial contraction of the low pressure system, with the maximum increase of SLP reaching 12 hPa over the eastern North Pacific (Fig. 6c) and the NPI increased by 4.1 hPa (Fig. 6d). In both the CAM3.1–$4CO_2$ and CAM3.1–$4CO_2$-GUW runs, however, the winter LOTC was significantly weakened by −2.6° and −2.8°C, respectively (Fig. 6e). Therefore, results of the idealized experiments demonstrate that the El Niño–like warming pattern of tropical time-mean SST is a critical forcing, which overwhelms the dampening effect of a weakened wintertime LOTC, in driving the intensification of the Aleutian low under greenhouse warming.

The dynamics underlying the modification of Aleutian low by the El Niño–like SST warming pattern is supposed to be analogous to the formation mechanism of PNA-like pattern of extratropical atmospheric circulation in response to ENSO, in which the tropical precipitation change is a key trigger (e.g., Trenberth et al. 1998; Lu et al. 2004). Here we further examined the responses of winter precipitation in the sensitivity experiments with CAM3.1, which well captures the spatial features of the mean state of winter precipitation in observation (Fig. 7a). In the CAM3.1–4CO2 run (Fig. 7b), the projected change pattern of precipitation is generally similar to that in CMIP5 models (Collins et al. 2013), especially in regard to more precipitation over the equatorial Pacific Ocean, which is absent in the CAM3.1–4CO2-GUW run (Fig. 7c). This can be explained by the "warmer-get-wetter" mechanism, which emphasizes the important effect of SST pattern change on precipitation in the tropics (Xie et al. 2010). Indeed, Fig. 7d further demonstrates that the spatial distribution of tropical precipitation change induced by the El Niño–like SST warming, particularly with large increases over the central-to-eastern equatorial Pacific Ocean and decreases over the Maritime Continent, resembles the classical pattern of precipitation anomalies driven by El Niño events (Dai and Wigley 2000). Correspondingly, the extratropical SLP change in space forced by the El Niño–like SST warming exhibits a PNA-like pattern (recall Fig. 6b). Hence, the El Niño–like SST warming pattern is expected to force a planetary wave train, akin
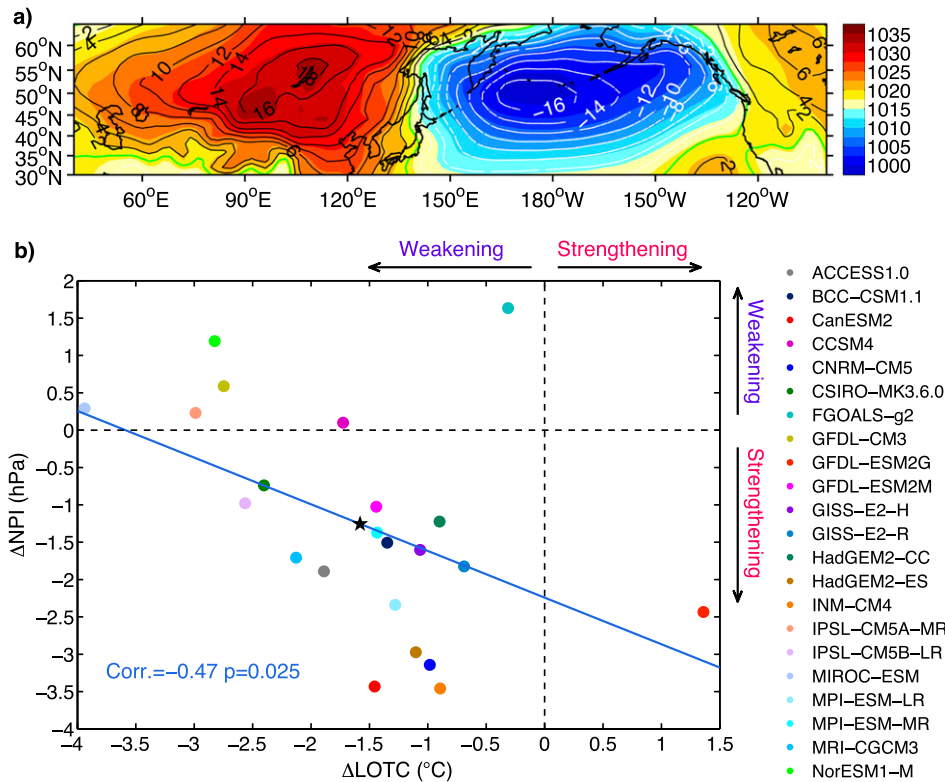
FIG. 4. (a) The climatological mean of winter SLP (hPa) from 1950 to 1999 (color shading), along with the deviation from the zonal mean (contour) based on the 20CRv2 reanalysis data. Green contour signifies the zero isoline. (b) Scatter diagram of the projected changes in the NPI vs changes in the winter LOTC over the North Pacific Ocean and the Asian continent in 22 models. ΔLOTC and ΔNPI are derived from the 50-yr-interval difference between the RCP8.5 run and historical run. A negative ΔLOTC and ΔNPI indicate a weakening of the winter LOTC and a strengthening of the Aleutian low, respectively. A blue line denotes the linear regression and an asterisk denotes the MMEM.

to the positive phase of PNA, through latent heat release in tropical precipitation and in turn intensify the Aleutian low. Meanwhile, the SST warming pattern also modulates precipitation change at midlatitudes: a substantial decrease of 20%–60% change over coastal Asia and the Bering Sea is accompanied by an increase of 20%–50% change over the eastern North Pacific, relative to the response to global uniform warming (Fig. 7d). This can be understood in the context of moisture flux changes driven by the intensified basin-scale cyclonic flow associated with the deepening of the Aleutian low.

5. Uncertainty in the twenty-first-century projection of Aleutian low

Although most models project the deepening of the Aleutian low, the magnitude is subject to intermodel diversity and even a few models project the opposite (recall Fig. 3a). In addition, the projection of winter SLP in space also exhibits weak robustness over the band of

30°–45°N and the southeastern part of the North Pacific (recall Fig. 3d). Indeed, Fig. 8 clearly illustrates that the maximum intermodel variance (referred to as model uncertainty) of the winter SLP projections across 22 models occurs to the southeast of the Aleutian Islands, where the intermodel spread is larger than the ensemble mean change and fewer than 17 models agree on the sign of change. A tail of large uncertainty also extends northwestward, with a second peak over the Bering Sea. Given the finding in section 4, it is expected that intermodel differences in the tropical Pacific SST warming pattern and the midlatitude LOTC projection are coupled with that in the winter SLP projection. Here we attempt to quantify contributions of such two sources to model uncertainty in the twenty-first-century projection of Aleutian low, based on intermodel singular value decomposition (SVD) and intermodel regression across 22 models. These intermodel analyses are similar to traditional methods, but with sampling performed across model space instead of across time to identify patterns linked to model discrepancies.
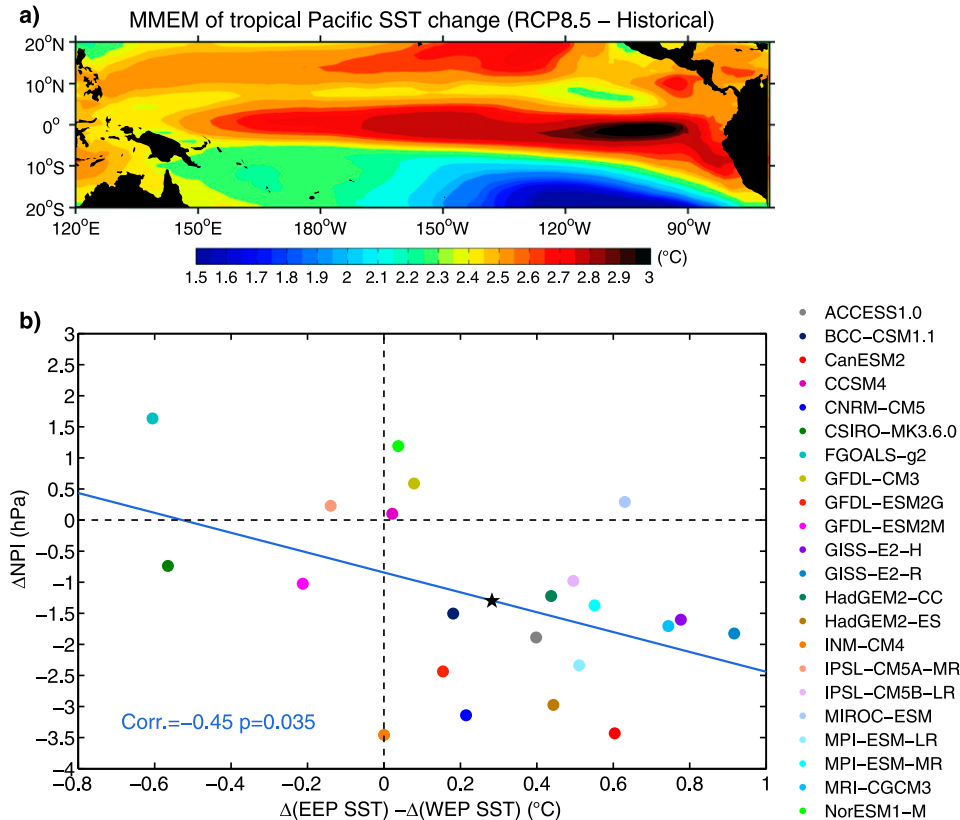
FIG. 5. (a) The MMEM of the tropical Pacific SST changes between the 50-yr RCP8.5 run and historical run in winter. Note that all models show SST warming significant at the 95% confidence level based on a two-tailed Student's t test. (b) Scatter diagram of the projected changes in the NPI vs changes in the equatorial Pacific east–west SST gradient in 22 models. A positive SST gradient indicates an El Niño–like response in a warmer climate. A blue line denotes the linear regression and an asterisk denotes the MMEM.

The influence of intermodel difference in the tropical Pacific SST warming pattern on model uncertainty in the winter SLP projection over the North Pacific is explicated based on the intermodel SVD analysis. The intermodel SVD is applied to the SLP changes over the region 30°–70°N, 130°E–120°W and the normalized tropical Pacific SST changes. To highlight uncertainty in spatial pattern, we normalized the tropical Pacific SST change with the tropical-mean (20°S–20°N, 120°E–70°W) SST warming in each model. The patterns of the first leading SVD mode, with a squared covariance fraction of 63.7%, are depicted by regressing SLP and SST changes onto the SST expansion coefficient, illustrating the influence of tropical Pacific Ocean on the midlatitude atmosphere (Fig. 9).

The homogeneous SST map (Fig. 9b) displays the enhanced warming in the central and eastern equatorial Pacific, with a peak located between 120° and 150°W. This pattern primarily reflects intermodel difference in the El Niño–like SST warming pattern, as the SST

expansion coefficient is closely related to Δ(EEP SST) $-$ Δ(WEP SST) with a correlation coefficient of 0.62 ($P = 0.002$). The heterogeneous SLP map (Fig. 9a) shows a zonal dipole over the tropical Pacific, characterizing a weakening of Walker circulation coupled with the El Niño–like SST warming pattern, and a teleconnection to the North Pacific—particularly, a swath of significantly decreased SLP extending from the Bering Sea to the eastern North Pacific, with a center of -1.25 hPa over the Bering Sea. Such a heterogeneous SLP pattern over the North Pacific indeed resembles the intermodel variance pattern of winter SLP projection (Fig. 8), with spatial correlation of 0.76 in absolute term.

Furthermore, we estimated the fraction of intermodel variance of winter SLP changes explained by the SST expansion coefficient, which is measured by the coefficient of determination (R^2) by performing the intermodel regression. About 35% of intermodel variance of SLP changes over the Bering Sea, where model uncertainty in space shows a second peak, is accounted for
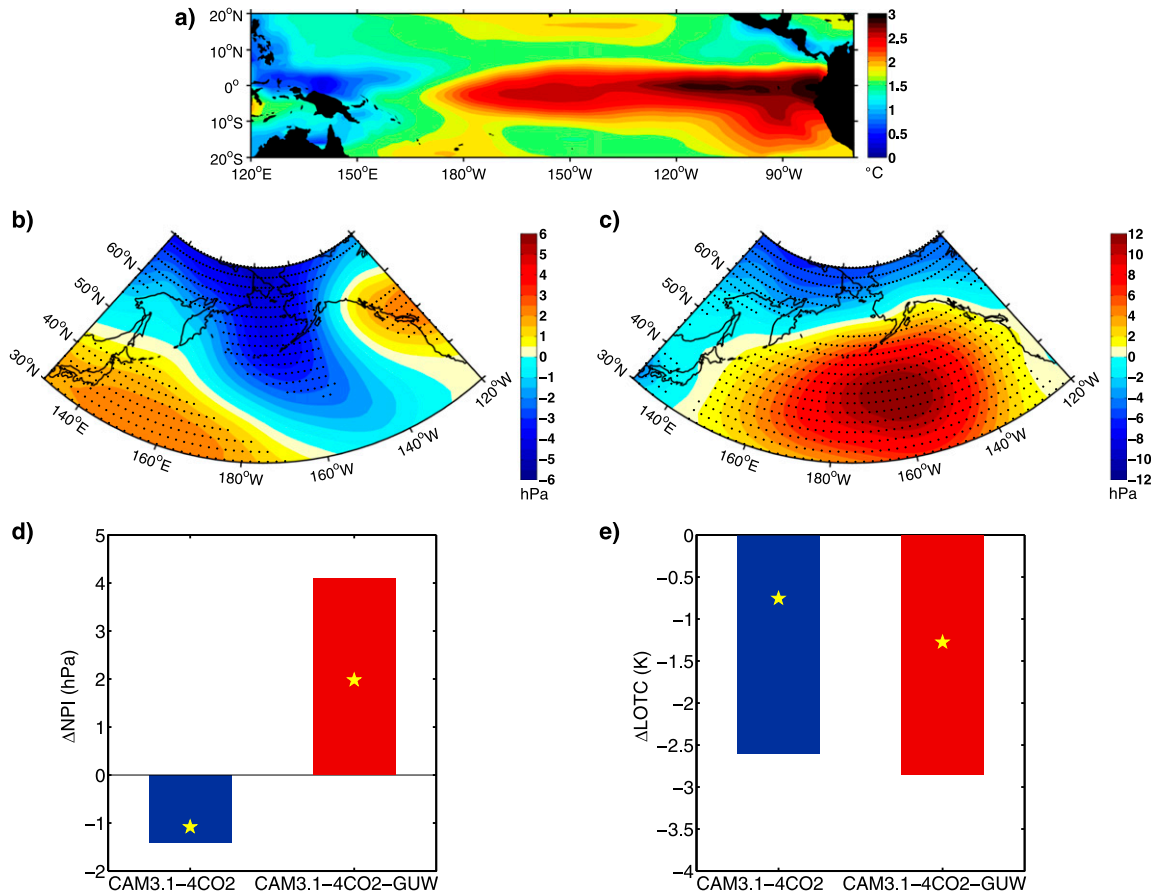
FIG. 6. (a) The climatological-mean tropical Pacific SST change between the winter equilibrium states (the last 50 yr) of the CAM3.1-RGO-4CO2 and CAM3.1-RGO-CTRL. Note that SST warming at each grid is significant at the 95% confidence level based on a two-tailed Student's t test. The climatological-mean winter SLP change based on the equilibrium-states (the last 50 yr) difference in terms of (b) CAM3.1–4CO2 minus CAM3.1-CTRL and (c) CAM3.1–4CO2-GUW minus CAM3.1-CTRL. Stippling indicates regions where SLP change is significant at the 95% confidence level. Also shown are the corresponding 50-yr differences in the winter (d) NPI and (e) LOTC. Blue and red bars represent CAM3.1–4CO2 minus CAM3.1-CTRL and CAM3.1–4CO2-GUW minus CAM3.1-CTRL, respectively. An asterisk denotes the 95% confidence level.

by intermodel difference in the tropical Pacific SST warming pattern (see Fig 11a). Such SST warming difference also explains about 23% of model uncertainty in the projection of Aleutian low intensity (i.e., ΔNPI), according to the significant correlation coefficient of -0.48 ($P = 0.02$) between the SST expansion coefficient and ΔNPI among models. By analyzing 17 CMIP3 models, Delcambre et al. (2013) also found that ENSO-like mean winter SST changes explain 30% of intermodel variance of the twenty-first-century projections of winter upper-level zonal wind at midlatitudes.

Next, we focused on intermodel difference in the LOTC projection (ΔLOTC) and regressed the projections of SAT and SLP onto ΔLOTC across models. The intermodel regressions of SAT (Fig. 10a) show less warming over the Asian continent and greater warming over the Bering Sea, which corresponds to a smaller

decrease of ΔLOTC relative to its MMEM decrease (-1.6°C) among models. Concurrently, the intermodel regressions of SLP (Fig. 10b) shows higher pressure over the Asian continent, with significant increase at high latitudes, and lower pressure over the North Pacific Ocean, with a well-defined center of decrease (-1.25 hPa) to the south of the Aleutian Islands. There is a possibility that less SAT warming over the Asian continent, which dominates the lessened ΔLOTC decrease and is dynamically associated with the local higher SLP, induces a relatively larger deepening of the Aleutian low.

To further look into the relative importance of different warming amplitudes over the Asian continent and the North Pacific Ocean to intermodel diversity in the Aleutian low projection, we regressed the SLP change onto the normalized ΔSAT_{Ocean}(40°–60°N, 170°E–150°W) and $-\Delta SAT_{Land}$(40°–60°N, 80°–120°E) across models,
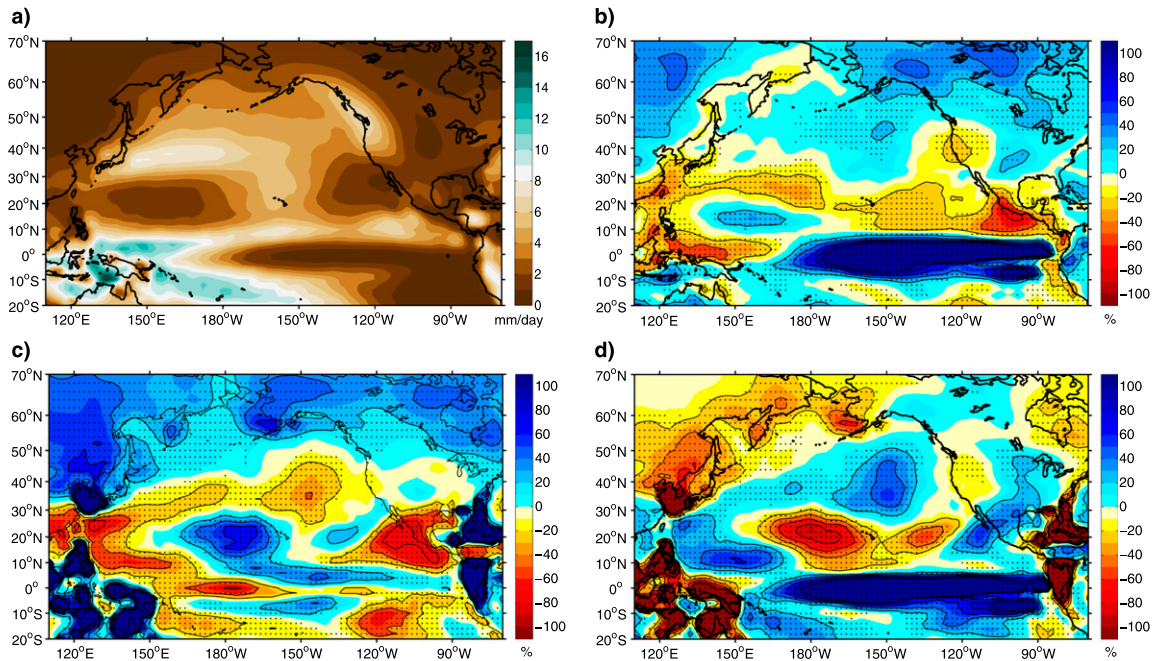
FIG. 7. (a) The winter precipitation pattern simulated in the CAM3.1-CTRL run. (b) The climatological-mean (last 50 yr) winter precipitation changes in percentage for CAM3.1–4CO2 relative to CAM3.1-CTRL. (c) As in (b), but for CAM3.1–4CO2-GUW. (d) The difference between (b) and (c). Contour interval in (b)–(d) is 20% change. Stippling indicates regions where precipitation change is significant at the 95% confidence level.

respectively, based on the definition of LOTC. As we expected, $-\Delta SAT_{Land}$ is found to have a higher correlation than ΔSAT_{Ocean} with $\Delta LOTC$ among models. In addition, over the North Pacific, the spatial distribution of SLP change difference associated with $-\Delta SAT_{Land}$ difference (Fig. 10c) is more similar to the intermodel variance pattern of winter SLP projection (Fig. 8) than that associated with ΔSAT_{Ocean} (Fig. 10d), as the spatial correlation for the former is higher than the latter (i.e., 0.76 vs 0.62 in absolute terms). Therefore, the intermodel difference in surface warming amplitude over the Asian continent is of greater importance than that over the North Pacific Ocean to intermodel diversity in the Aleutian low projection. Figure 11b further illustrates that the $-\Delta SAT_{Land}$ difference explains about 50% of intermodel variance of SLP changes over the central North Pacific, where the maximum model uncertainty exists. Also, we found that the correlation coefficient between $-\Delta SAT_{Land}$ and ΔNPI among models is -0.56 ($P = 0.007$), which suggests that intermodel difference in surface warming amplitude over the Asian continent explains about 31% of model uncertainty in the projection of Aleutian low intensity.

In summary, the results above show that intermodel differences in the spatial pattern of tropical Pacific SST warming and the midlatitude LOTC projection explain

about 35% and 50% of large uncertainty in the winter SLP projection over the Bering Sea and the central North Pacific, respectively. Furthermore, the difference in the surface warming amplitude over the Asian continent makes a greater contribution than that in the tropical Pacific SST warming pattern to model uncertainty in the twenty-first-century projection of Aleutian low intensity. It should be noted that the model uncertainty in this study, which is measured as the intermodel spread for models with single ensemble member, contains uncertainty due to model framework and representations of internal variability. Hence, internal atmospheric variability, such as the northern annular mode, should be another strong source of
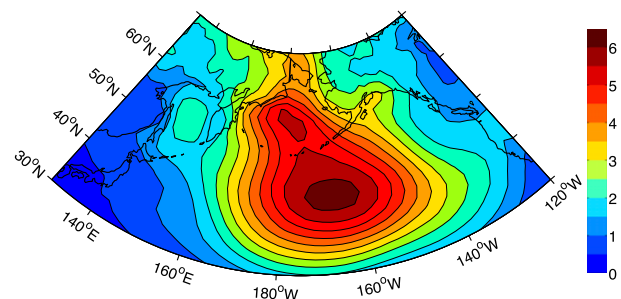

FIG. 8. The intermodel variance of winter SLP changes (hPa$_2$) between the 50-yr RCP8.5 run and historical run across 22 models.
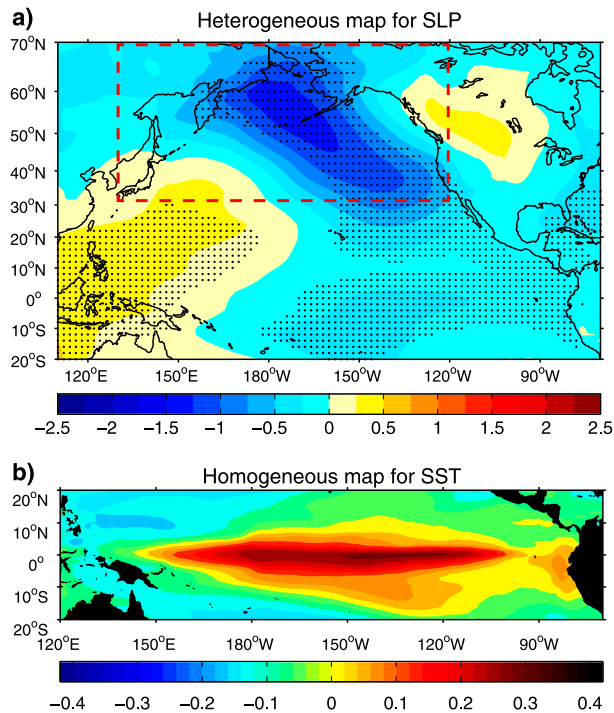
FIG. 9. The patterns of intermodel covariability between the projected changes in the Pacific SLP and the tropical Pacific SST in winter, derived by regressing SLP change (hPa) and SST change onto the SST expansion coefficient taken from the first mode of intermodel SVD. Note that the SLP domain used for the SVD analysis is confined to the North Pacific region denoted by a red dashed line, but a larger domain including tropical Pacific is used for SLP regression. Stippling indicates regression significant at the 95% confidence level. Note that SST change is normalized by the tropical-mean (20°S–20°N, 120°E–70°W) SST warming in each model.

uncertainty in the wintertime SLP projection at midlatitudes (Deser et al. 2012; Oshima et al. 2012).

6. Discussion

a. Influence of Arctic sea ice loss on the Aleutian low change

Given that a smaller decrease of ΔLOTC (which is dominated by less warming over the Asian continent) is associated with greater SAT warming over the Bering Sea (Fig. 10a), where sea ice melts as a consequence of warming, we may expect that there is a potential relationship between intermodel differences in SAT warming over the Asian continent and SIC reduction in the Bering Sea. Further inspection indeed shows that $-\Delta$SAT$_{\text{Land}}$ is significantly correlated with SIC reduction in the Bering Sea across models, with correlation coefficient of -0.58 ($P = 0.004$). It seems reasonable to suggest that a model with less warming over the Asian continent tends to project a relatively larger deepening of

the Aleutian low, which results in the enhanced SAT warming over the Bering Sea through inducing a stronger basin-scale cyclonic flow and in turn leads to a greater reduction of sea ice in the Bering Sea.

On the other hand, sea ice melt has been found to substantially affect the atmospheric circulation on both regional and global scales (e.g., Deser et al. 2010b; Peings and Magnusdottir 2014). In addition, the spatial distribution of sea ice loss in winter primarily occurs not only in the Bering Sea, but also in other marginal seas, such as Okhotsk and Chukchi Seas in the Pacific, as well as Greenland, Labrador, and Barents–Kara Seas and Hudson Bay in the Atlantic (Fig. 12a). Thus an issue arises as to whether the Arctic sea ice loss plays a role in the intensification of the Aleutian low in a warmer climate. To look into this matter, we compared ΔNPI with SIC reduction averaged in the regions of the entire Arctic (50°–90°N) and the Pacific (50°–70°N, 140°E–150°W) and Atlantic (50°–84°N, 96°W–100°E) sectors across models, respectively. It is found that SIC reduction in any region is not statistically correlated with the NPI change, implying that the influence of sea ice loss on SLP is likely to be limited and very local.

Given that, we further examined the influence of sea ice loss in the Pacific region on local SAT and SLP based on the intermodel regression analysis. As shown in Figs. 12b and 12c, results demonstrate that the greater surface warming and lower SLP over the Okhotsk and Bering Seas coincide with the local larger SIC reduction. It can be conjectured that sea ice loss in the Pacific warms surface air through vertical diffusion of upward turbulent heat fluxes and in turn induces a decrease of local SLP as a linear dynamic response to the diabatic heating, as suggested by Deser et al. (2010b). The fact that the low pressure over the Okhotsk and Bering Seas deepens as the underlying sea ice cover declines is also confirmed by the scatter diagram of Fig. 12d. Therefore, our diagnosis suggests that the wintertime sea ice loss within the marginal seas of the Pacific contributes to the deepening of local low pressure rather than the Aleutian low pressure systems. However, results of sensitivity experiments with an atmospheric model (e.g., Singarayer et al. 2006; Sun et al. 2015) or a fully coupled model (Deser et al. 2016) seem to suggest different spatial distributions of negative SLP anomalies over the North Pacific in response to the prescribed Arctic sea ice loss. The influence of Arctic sea ice loss on regional atmospheric circulation thus needs to be further clarified.

b. Difference in the centennial trend of NPI between observation and CMIP5 historical simulations

In section 3a, we find that the long-term trend of NPI in the twentieth century has decreased by approximately -1.5 hPa on the average of five observations since 1911, which, however, is double that for the MMEM of the
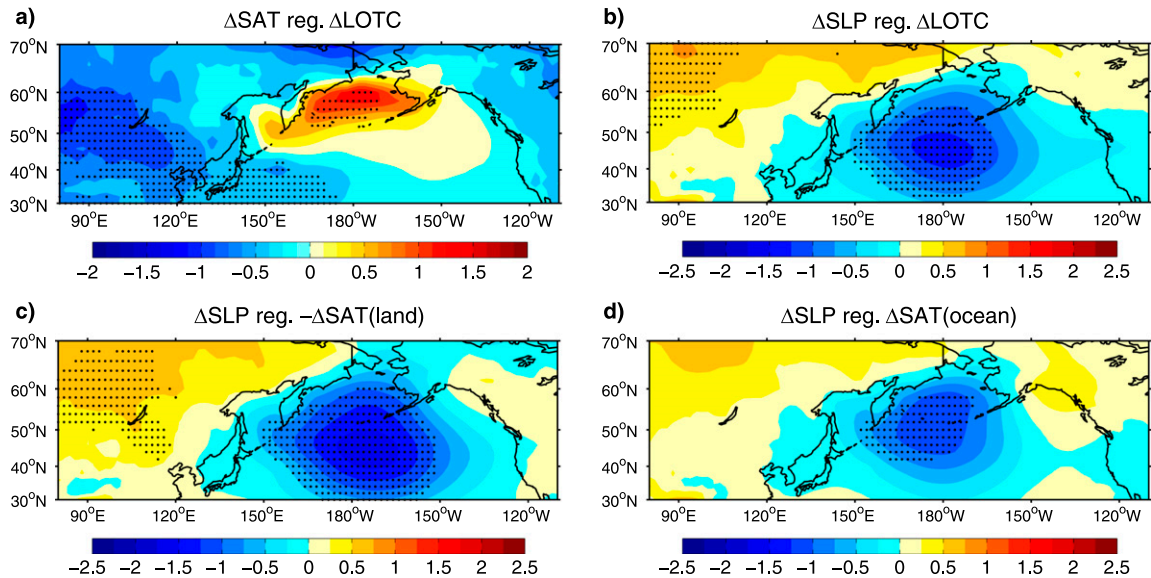
FIG. 10. Intermodel regression patterns of the projected changes in (a) SAT (°C) and (b) SLP (hPa) onto the LOTC changes in winter. (c),(d) As in (b), but for regressions onto the normalized SAT changes over the Asian continent and the North Pacific Ocean, respectively. Here SAT changes are normalized by the domain-mean (30°–70°N, 80°E–120°W) SAT warming in each model. Stippling indicates regression significant at the 95% confidence level.

historical simulations. Owing to large variability on interannual to multidecadal time scales, natural internal variability is likely to be involved in the strong long-term decrease of NPI in observation. Those interannual to multidecadal fluctuations, however, must be canceled out in the MMEM times series of NPI (Fig. 2c). Therefore, the NPI change induced by the anthropogenic warming in observation is likely to be smaller than or comparable to the MMEM.

By looking into the performance of each model, most models are found to agree on the sign of the downward NPI centennial trend, but only five models produce significant trends larger than or comparable to the observation. This could be in part due to the model

deficiencies in producing a significant El Niño–like warming trend of the tropical Pacific SST, as inferred from the weak increasing tendency of equatorial Pacific east–west SST gradient captured by most CMIP5 models (Fig. 13). It should be noted that a significant centennial trend of $0.1°C (100 yr)^{-1}$ is detected based on the MMEM time series of east–west SST gradient anomalies, which indicates an El Niño–like warming tendency and coincides with a deepening tendency of the climatological-mean Aleutian low (Fig. 2c). This implies a driving role of the tropical El Niño–like warming in the strengthening of the Aleutian low during the twentieth century. Other possible reasons include underestimations of the modeled atmospheric teleconnection forced by the natural
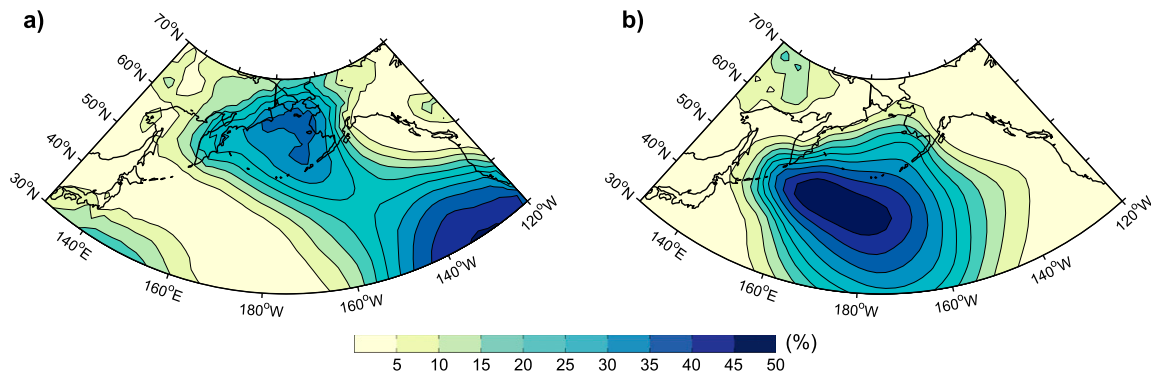

FIG. 11. The fraction (%) of intermodel variance of winter SLP changes explained by (a) the tropical Pacific SST expansion coefficient taken from the first mode of intermodel SVD and (b) the normalized SAT changes over the Asian continent (i.e., −ΔSATLand). See section 5 for details.
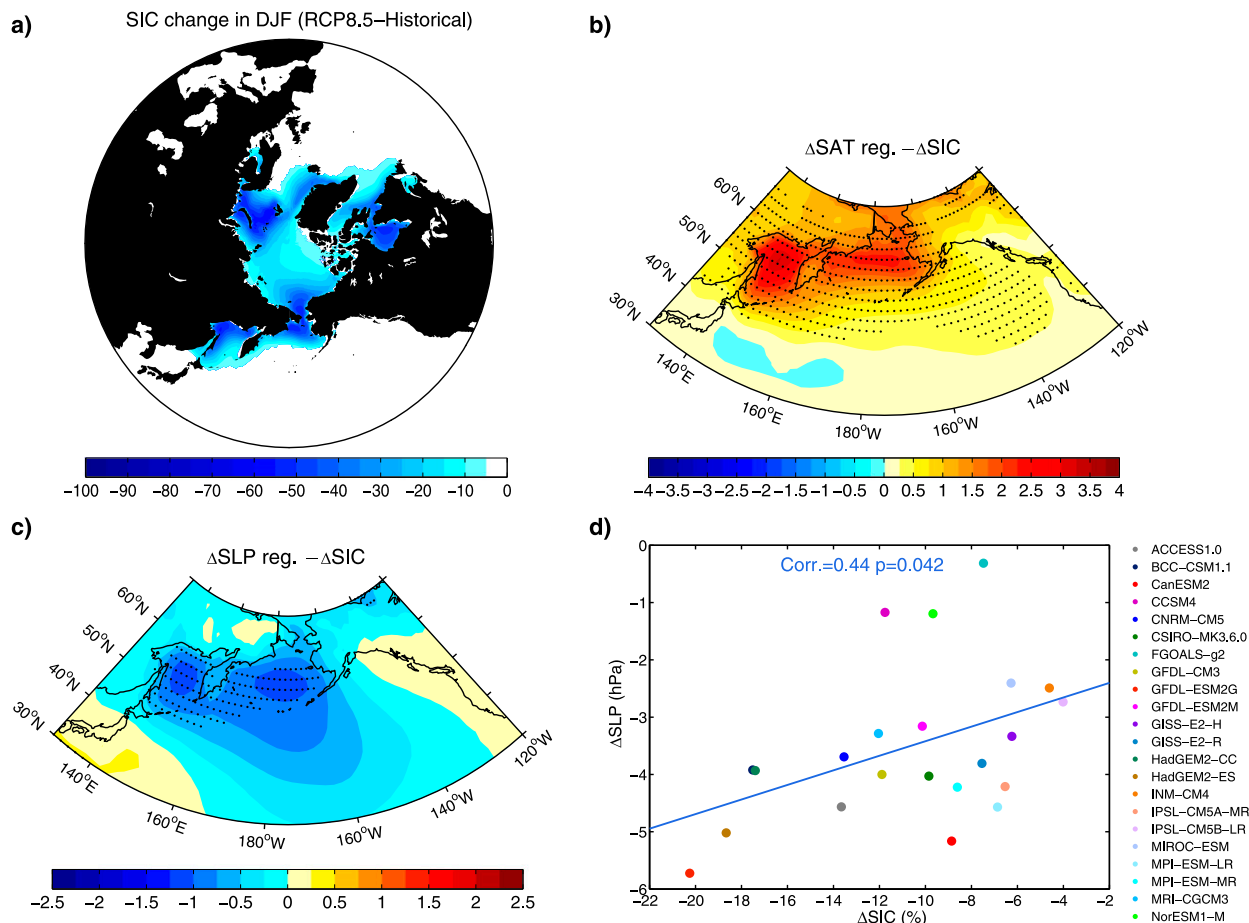
FIG. 12. (a) The MMEM of Arctic SIC changes (%) in winter between the 50-yr RCP8.5 run and historical run. (b) Intermodel regression pattern of the winter SAT projection (°C) onto the area-averaged SIC reduction in the Pacific [ΔSIC (50°–70°N, 140°E–150°W)]. (c) As in (b), but for the winter SLP (hPa). Stippling indicates regression significant at the 95% confidence level. Note that the time series of SIC reduction has been reversed and normalized so that the regressions are associated with one standard deviation of intermodel spread. (d) Scatter diagram of the projected SLP changes averaged in the region of (50°–66°N, 140°E–150°W) vs ΔSIC in 22 models. The blue line denotes the linear regression.

variability of the tropical Pacific SST, as suggested by Furtado et al. (2011), and variabilities of midlatitude atmospheric planetary-scale waves, since more than 60% of models undervalue the interannual standard deviation of the NPI (recall Table 3). Previous studies also have found that the simulated SLP trends over the Northern Hemisphere are much lower in magnitude than its observed counterpart during the second half of the twentieth century, which is suggested to be attributable to an underestimation of the simulated SLP response to external forcing and/or an inherent limitation in hindcasting the internal variability of atmospheric circulation (Gillett et al. 2005; Wallace et al. 2012).

c. Some implications

As for the long-term trend of tropical Pacific SST over the twentieth century, various historical SST datasets display either an El Niño–like or a La Niña–like SST warming pattern (Deser et al. 2010a; Vecchi et al. 2008). While it is difficult to distinguish which pattern is correct from the limited SST datasets, the intensification of the Aleutian low, which is more robust during the twentieth century, seems to support the notion of an El Niño–like warming in the tropical Pacific Ocean. In fact, Tokinaga et al. (2012) have reconstructed an SST dataset for the period of 1950–2009, which reduces biases caused by changes in SST measurement technique, and pointed out that the resulting trend pattern features a reduced zonal gradient between the eastern Pacific and the western Pacific/southeastern Indian Ocean.

The deepening of the Aleutian low in a warming climate may result in substantial changes of the temperature extremes in the Pacific Rim region, such as more warm extremes over large parts of northern North
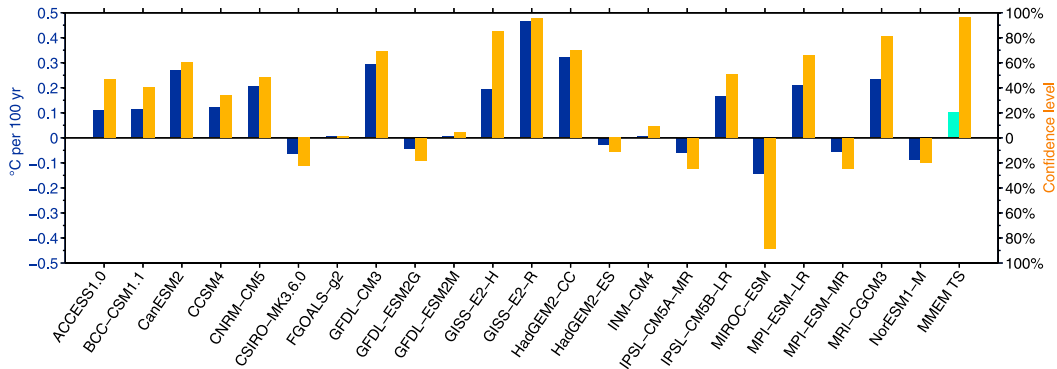
FIG. 13. The centennial trends of the winter equatorial Pacific east–west SST gradient anomalies (i.e., EEP minus WEP SST anomalies) in the historical simulations of 22 models. MMEM TS denotes the MMEM time series of east–west SST gradient anomalies. Trend and its statistical significance are estimated with the Sen median slope and the modified Mann–Kendall trend, respectively.

America (especially the northwest area and Alaska) and more cold extremes over eastern Asia, as inferred from Kenyon and Hegerl (2008). Recent study also indicates that subtropical western boundary currents are accelerating, which leads to the formation of oceanic hotspots over the subarctic frontal zones (Wu et al. 2012). In conjunction with the enhancement of the summertime subtropical Pacific high (Li et al. 2012), the intensification of the wintertime Aleutian low can provide an important driving mechanism for the acceleration of the subtropical gyre circulation as the climate warms.

7. Summary

Analysis of CMIP5 multimodel historical simulations and RCP8.5 projections illustrates an intensification and northward expansion of the Aleutian low in response to greenhouse warming, which is manifested in the significant decrease of multimodel-averaged NPI by approximately −1.3 hPa or approximately −0.4 hPa per 1°C of global surface warming (62% larger than the unforced internal variability of the NPI) and the central area with SLP lower than 999.0 hPa expanded about 7 times that in the twentieth century. As for the projected change in space, the low pressure system to north of 45°N except over the western coast of North American displays a highly robust intensification, with the maximum decrease of SLP reaching −5.5 hPa over the northern Bering Sea.

It is demonstrated that the deepening of the Aleutian low can be driven by an El Niño–like warming in the tropical Pacific Ocean, with the enhanced SST warming in the eastern equatorial Pacific, which overshadows the effect of the weakened winter LOTC that dampens the Aleutian low change under greenhouse forcing. Salathé (2006) noted that the response of Aleutian low to greenhouse warming is consistent with the northward shift and

intensification of storm tracks at midlatitudes, indicating an active role of storm tracks in modulating Aleutian low changes. However, it seems difficult to establish a cause-and-effect relationship between them due to the eddy–mean flow interaction. Thus as a remote forcing, the El Niño–like SST warming in the tropical Pacific is of great importance to the intensification of the Aleutian low under greenhouse warming. The Atlantic Ocean might also remotely modulate the Aleutian low response, as a shutdown of the Atlantic meridional overturning circulation likely results in a strengthening of the Aleutian low (e.g., Zhang and Delworth 2007; Wu et al. 2008). Further modeling studies are warranted to clarify role of the Atlantic Ocean changes played in the projections of atmospheric circulation over the North Pacific in a warmer climate.

While the projected deepening of the Aleutian low on multimodel average is robust, individual model portrayals vary primarily in magnitude. It is found that intermodel differences in the spatial pattern of tropical Pacific SST warming and the midlatitude LOTC projection explain about 35% and 50% of large uncertainty in the winter SLP projection over the Bering Sea and the central North Pacific, respectively. Particularly, a greater contribution to model uncertainty in the projection of Aleutian low intensity comes from intermodel difference in the LOTC projection, which is dominated by difference in the surface warming amplitude over the Asian continent. It remains uncertain what is responsible for model uncertainty in the wintertime surface warming amplitude over the Asian continent. One possible source could be intermodel diversity in the projected Arctic sea ice loss in late autumn, which is suggested to drive terrestrial cooling across Eurasia (Deser et al. 2016).

REFERENCES

Alexander, M. A., I. Bladé, M. Newman, J. R. Lanzante, N. C. Lau, and J. D. Scott, 2002: The atmospheric bridge: The influence of ENSO teleconnections on air–sea interaction over the global oceans. *J. Climate*, **15**, 2205–2231, doi:10.1175/1520-0442(2002)015<2205:TABTIO>2.0.CO;2.

Allan, R., and T. Ansell, 2006: A new globally complete monthly historical gridded mean sea level pressure dataset (HadSLP2): 1850–2004. *J. Climate*, **19**, 5816–5842, doi:10.1175/JCLI3937.1.

An, S.-I., J.-W. Kim, S.-H. Im, B.-M. Kim, and J.-H. Park, 2012: Recent and future sea surface temperature trends in tropical Pacific warm pool and cold tongue regions. *Climate Dyn.*, **39**, 1373–1383, doi:10.1007/s00382-011-1129-7.

Andrews, D. G., J. R. Holton, and C. B. Leovy, 1987: *Middle Atmosphere Dynamics*. Elsevier, 489 pp.

Boer, G. J., G. Flato, and D. Ramsden, 2000: A transient climate change simulation with greenhouse gas and aerosol forcing: Projected climate to the twenty-first century. *Climate Dyn.*, **16**, 427–450, doi:10.1007/s003820050338.

Chavez, F. P., J. Ryan, S. E. Lluch-Cota, and C. M. Ñiquen, 2003: From anchovies to sardines and back: Multidecadal change in the Pacific Ocean. *Science*, **299**, 217–221, doi:10.1126/science.1075880.

Chiang, J. C. H., Y. Fang, and P. Chang, 2008: Interhemispheric thermal gradient and tropical Pacific climate. *Geophys. Res. Lett.*, **35**, L14704, doi:10.1029/2008GL034166.

Clement, A. C., R. Seager, M. A. Cane, and S. E. Zebiak, 1996: An ocean dynamical thermostat. *J. Climate*, **9**, 2190–2196, doi:10.1175/1520-0442(1996)009<2190:AODT>2.0.CO;2.

Collins, M. R., and Coauthors, 2013: Long-term climate change: Projections, commitments and irreversibility. *Climate Change 2013: The Physical Science Basis*, T. F. Stocker et al., Eds., Cambridge University Press, 1029–1136.

Collins, W. D., and Coauthors, 2006: The formulation and atmospheric simulation of the Community Atmospheric Model version 3: CAM3. *J. Climate*, **19**, 2144–2161, doi:10.1175/JCLI3760.1.

Compo, G. P., and Coauthors, 2011: The Twentieth Century Reanalysis project. *Quart. J. Roy. Meteor. Soc.*, **137**, 1–28, doi:10.1002/qj.776.

Dai, A., and T. M. L. Wigley, 2000: Global patterns of ENSO-induced precipitation. *Geophys. Res. Lett.*, **27**, 1283–1286, doi:10.1029/1999GL011140.

Delcambre, S. C., D. J. Lorenz, D. J. Vimont, and J. E. Martin, 2013: Diagnosing Northern Hemisphere jet portrayal in 17 CMIP3 global climate models: Twenty-first-century projections. *J. Climate*, **26**, 4930–4946, doi:10.1175/JCLI-D-12-00359.1.

Deser, C., and A. S. Phillips, 2009: Atmospheric circulation trends, 1950–2000: The relative roles of sea surface temperature forcing and direct atmospheric radiative forcing. *J. Climate*, **22**, 396–413, doi:10.1175/2008JCLI2453.1.

——, ——, and J. W. Hurrell, 2004: Pacific interdecadal climate variability: Linkages between the tropics and North Pacific during boreal winter since 1900. *J. Climate*, **17**, 3109–3124, doi:10.1175/1520-0442(2004)017<3109:PICVLB>2.0.CO;2.

——, ——, and M. A. Alexander, 2010a: Twentieth century tropical sea surface temperature trends revisited. *Geophys. Res. Lett.*, **37**, L10701, doi:10.1029/2010GL043321.

——, R. Tomas, M. A. Alexander, and D. Lawrence, 2010b: The seasonal atmospheric response to projected Arctic sea ice loss in the late twenty-first century. *J. Climate*, **23**, 333–351, doi:10.1175/2009JCLI3053.1.

——, A. Phillips, V. Bourdette, and H. Teng, 2012: Uncertainty in climate change projections: The role of internal variability. *Climate Dyn.*, **38**, 527–546, doi:10.1007/s00382-010-0977-x.

——, L. Sun, R. A. Tomas, and J. Screen, 2016: Does ocean coupling matter for the northern extratropical response to projected Arctic sea ice loss? *Geophys. Res. Lett.*, **43**, 2149–2157, doi:10.1002/2016GL067792.

Fang, Y., 2005: A coupled model study of the remote influence of ENSO on tropical Atlantic SST variability. Ph.D. thesis, Texas A&M University, 93 pp.

Furtado, J. C., E. Di Lorenzo, N. Schneider, and N. A. Bond, 2011: North Pacific decadal variability and climate change in the IPCC AR4 models. *J. Climate*, **24**, 3049–3067, doi:10.1175/2010JCLI3584.1.

Gillett, N. P., F. W. Zwiers, A. J. Weaver, and P. A. Stott, 2003: Detection of human influence on sea level pressure. *Nature*, **422**, 292–294, doi:10.1038/nature01487.

——, R. J. Allan, and T. J. Ansell, 2005: Detection of external influence on sea level pressure with a multi-model ensemble. *Geophys. Res. Lett.*, **32**, L19714, doi:10.1029/2005GL023640.

Hamed, K. H., and A. R. Rao, 1998: A modified Mann-Kendall trend test for autocorrelated data. *J. Hydrol.*, **204**, 182–196, doi:10.1016/S0022-1694(97)00125-X.

Hollowed, A. B., S. R. Hare, and W. S. Wooster, 2001: Pacific Basin climate variability and patterns of northeast Pacific marine fish production. *Prog. Oceanogr.*, **49**, 257–282, doi:10.1016/S0079-6611(01)00026-X.

Honda, M., S. Yamane, and H. Nakamura, 2005: Impacts of the Aleutian–Icelandic low seesaw on the surface climate during the twentieth century. *J. Climate*, **18**, 2793–2802, doi:10.1175/JCLI3419.1.

Hori, M. E., and H. Ueda, 2006: Impact of global warming on the eastern Asian winter monsoon as revealed by nine coupled atmosphere–ocean GCMs. *Geophys. Res. Lett.*, **33**, L03713, doi:10.1029/2005GL024961.

Jia, F., and L. Wu, 2013: A study of response of the equatorial Pacific SST to doubled-CO_2 forcing in the coupled CAM–1.5-layer reduced-gravity ocean model. *J. Phys. Oceanogr.*, **43**, 1288–1300, doi:10.1175/JPO-D-12-0144.1.

Kenyon, J., and G. C. Hegerl, 2008: Influence of modes of climate variability on global temperature extremes. *J. Climate*, **21**, 3872–3889, doi:10.1175/2008JCLI2125.1.

Kwon, Y., and C. Deser, 2007: North Pacific decadal variability in the Community Climate System Model version 2. *J. Climate*, **20**, 2416–2433, doi:10.1175/JCLI4103.1.

Latif, M., and T. P. Barnett, 1994: Causes of decadal climate variability over the North Pacific and North America. *Science*, **266**, 634–637, doi:10.1126/science.266.5185.634.

Lehodey, P., and Coauthors, 2006: Climate variability, fish and fisheries. *J. Climate*, **19**, 5009–5030, doi:10.1175/JCLI3898.1.

Li, W., L. Li, M. Ting, and Y. Liu, 2012: Intensification of Northern Hemisphere subtropical highs in a warming climate. *Nat. Geosci.*, **5**, 830–834, doi:10.1038/ngeo1590.

Livezey, R. E., and W. Y. Chen, 1983: Statistical field significance and its determination by Monte Carlo techniques. *Mon. Wea. Rev.*, **111**, 46–59, doi:10.1175/1520-0493(1983)111<0046:SFSAID>2.0.CO;2.

Lu, J., R. J. Greatbatch, and K. A. Peterson, 2004: Trend in Northern Hemisphere winter atmospheric circulation during the last half of the twentieth century. *J. Climate*, **17**, 3745–3760, doi:10.1175/1520-0442(2004)017<3745:TINHWA>2.0.CO;2.

Meehl, G. A., and W. M. Washington, 1996: El Niño–like climate change in a model with increased atmospheric CO_2 concentrations. *Nature*, **382**, 56–60, doi:10.1038/382056a0.

Oshima, K., Y. Tanimoto, and S.-P. Xie, 2012: Regional patterns of wintertime SLP change over the North Pacific and their uncertainty in CMIP3 multi-model projections. *J. Meteor. Soc. Japan*, **90A**, 385–396, doi:10.2151/jmsj.2012-A23.

Overland, J. E., and C. H. Pease, 1982: Cyclone climatology of the Bering Sea and its relation to sea ice extent. *Mon. Wea. Rev.*, **110**, 5–13, doi:10.1175/1520-0493(1982)110<0005:CCOTBS>2.0.CO;2.

——, J. M. Adams, and N. A. Bond, 1999: Decadal variability of the Aleutian low and its relation to high-latitude circulation. *J. Climate*, **12**, 1542–1548, doi:10.1175/1520-0442(1999)012<1542:DVOTAL>2.0.CO;2.

Peings, Y., and G. Magnusdottir, 2014: Response of the wintertime Northern Hemisphere atmospheric circulation to current and projected Arctic sea ice decline: A numerical study with CAM5. *J. Climate*, **27**, 244–264, doi:10.1175/JCLI-D-13-00272.1.

Pickart, R. S., G. W. K. Moore, A. M. Macdonald, I. A. Renfrew, J. E. Walsh, and W. S. Kessler, 2009: Seasonal evolution of Aleutian low pressure systems: Implications for the North Pacific subpolar circulation. *J. Phys. Oceanogr.*, **39**, 1317–1339, doi:10.1175/2008JPO3891.1.

Poli, P., and Coauthors, 2016: ERA-20C: An atmospheric reanalysis of the 20th century. *J. Climate*, **29**, 4083–4097, doi:10.1175/JCLI-D-15-0556.1.

Rodionov, S. N., J. E. Overland, and N. A. Bond, 2005: The Aleutian low and winter climatic conditions of the Bering Sea. Part I: Classification. *J. Climate*, **18**, 160–177, doi:10.1175/JCLI3253.1.

Salathé, E. P., Jr., 2006: Influences of a shift in North Pacific storm tracks on western North American precipitation under global warming. *Geophys. Res. Lett.*, **33**, L19820, doi:10.1029/2006GL026882.

Schneider, N., and B. D. Cornuelle, 2005: The forcing of the Pacific decadal oscillation. *J. Climate*, **18**, 4355–4373, doi:10.1175/JCLI3527.1.

Seager, R., Y. Kushnir, N. H. Naik, M. A. Cane, and J. Miller, 2001: Wind-driven shifts in the latitude of the Kuroshio–Oyashio Extension and generation of SST anomalies on decadal timescales. *J. Climate*, **14**, 4249–4265, doi:10.1175/1520-0442(2001)014<4249:WDSITL>2.0.CO;2.

Sen, P. K., 1968: Estimates of the regression coefficient based on Kendall's tau. *J. Amer. Stat. Assoc.*, **63**, 1379–1389, doi:10.1080/01621459.1968.10480934.

Singarayer, J. S., J. L. Bamber, and P. J. Valdes, 2006: Twenty-first-century climate impacts from a declining Arctic sea ice cover. *J. Climate*, **19**, 1109–1125, doi:10.1175/JCLI3649.1.

Smith, T. M., and R. W. Reynolds, 2004: Reconstruction of monthly mean oceanic sea level pressure based on COADS and station data (1854–1997). *J. Oceanic Atmos. Technol.*, **21**, 1272–1282, doi:10.1175/1520-0426(2004)021<1272:ROMMOS>2.0.CO;2.

Sueyoshi, M., and T. Yasuda, 2012: Inter-model variability of projected sea level changes in the western North Pacific in CMIP3 coupled climate models. *J. Oceanogr.*, **68**, 533–543, doi:10.1007/s10872-012-0117-9.

Sun, L., C. Deser, and R. A. Tomas, 2015: Mechanisms of stratospheric and tropospheric circulation response to projected Arctic sea ice loss. *J. Climate*, **28**, 7824–7845, doi:10.1175/JCLI-D-15-0169.1.

Taylor, K. E., R. J. Stouffer, and G. A. Meehl, 2012: An overview of CMIP5 and the experiment design. *Bull. Amer. Meteor. Soc.*, **93**, 485–498, doi:10.1175/BAMS-D-11-00094.1.

Terada, K., and M. Hanzawa, 1984: Climate of the North Pacific Ocean. *World Survey of Climatology*, Vol. 15, H. Van Loon, Ed., Elsevier, 431–504.

Tokinaga, H., S.-P. Xie, C. Deser, Y. Kosaka, and Y. M. Okumura, 2012: Slowdown of the Walker circulation driven by tropical Indo-Pacific warming. *Nature*, **491**, 439–443, doi:10.1038/nature11576.

Trenberth, K. E., and D. A. Paolino, 1980: The Northern Hemisphere sea-level pressure data set: Trends, errors and discontinuities. *Mon. Wea. Rev.*, **108**, 855–872, doi:10.1175/1520-0493(1980)108<0855:TNHSLP>2.0.CO;2.

——, and J. W. Hurrell, 1994: Decadal atmosphere–ocean variations in the Pacific. *Climate Dyn.*, **9**, 303–319, doi:10.1007/BF00204745.

——, G. W. Branstator, D. Karoly, A. Kumar, N.-C. Lau, and C. Ropelewski, 1998: Progress during TOGA in understanding and modeling global teleconnections associated with tropical sea surface temperatures. *J. Geophys. Res.*, **103**, 14 291–14 324, doi:10.1029/97JC01444.

Vecchi, G. A., A. Clement, and B. J. Soden, 2008: Examining the tropical Pacific's response to global warming. *Eos, Trans. Amer. Geophys. Union*, **89**, 81–83, doi:10.1029/2008EO090002.

Wallace, J. M., Y. Zhang, and L. Bajuk, 1996: Interpretation of interdecadal trends in Northern Hemisphere surface air temperature. *J. Climate*, **9**, 249–259, doi:10.1175/1520-0442(1996)009<0249:IOITIN>2.0.CO;2.

——, Q. Fu, B. V. Smoliak, P. Lin, and C. M. Johanson, 2012: Simulated versus observed patterns of warming over the extratropical Northern Hemisphere continents during the cold season. *Proc. Natl. Acad. Sci. USA*, **109**, 14 337–14 342, doi:10.1073/pnas.1204875109.

Wu, L., C. Li, C. Yang, and S.-P. Xie, 2008: Global teleconnections in response to a shutdown of the Atlantic meridional overturning circulation. *J. Climate*, **21**, 3002–3019, doi:10.1175/2007JCLI1858.1.

——, and Coauthors, 2012: Enhanced warming over the global subtropical western boundary currents. *Nat. Climate Change*, **2**, 161–166, doi:10.1038/nclimate1353.

Xie, S.-P., C. Deser, G. A. Vecchi, J. Ma, H. Teng, and A. T. Wittenberg, 2010: Global warming pattern formation: Sea surface temperature and rainfall. *J. Climate*, **23**, 966–986, doi:10.1175/2009JCLI3329.1.

——, and Coauthors, 2015: Towards predictive understanding of regional climate change. *Nat. Climate Change*, **5**, 921–930, doi:10.1038/nclimate2689.

Yamaguchi, K., and A. Noda, 2006: Global warming patterns over the North Pacific: ENSO versus AO. *J. Meteor. Soc. Japan*, **84**, 221–241, doi:10.2151/jmsj.84.221.

Yeh, S.-W., Y.-G. Ham, and J.-Y. Lee, 2012: Changes in the tropical Pacific SST trend from CMIP3 to CMIP5 and its implication of ENSO. *J. Climate*, **25**, 7764–7771, doi:10.1175/JCLI-D-12-00304.1.

Zebiak, S. E., and M. A. Cane, 1987: A model ENSO. *Mon. Wea. Rev.*, **115**, 2262–2278, doi:10.1175/1520-0493(1987)115<2262:AMENO>2.0.CO;2.

Zhang, R., and T. L. Delworth, 2007: Impact of the Atlantic multidecadal oscillation on North Pacific climate variability. *Geophys. Res. Lett.*, **34**, L23708, doi:10.1029/2007GL031601.